Brazilian Journal of Physics
ISSN: 0103-9733
luizno.bjp@gmail.com
Sociedade Brasileira de Física
Brasil

Badran, R. I.; Al-Lehyani, I. H.

An Analysis of Heavy-Ion Elastic Scattering Processes Using Numerical Model Based on the Partial Wave Parameterised S-Matrix with Regge Pole Factor

Brazilian Journal of Physics, vol. 46, núm. 3, 2016, pp. 341-354
Sociedade Brasileira de Física
São Paulo, Brasil

Braz J Phys (2016) 46:341–354
DOI 10.1007/s13538-016-0418-3

NUCLEAR PHYSICS

An Analysis of Heavy-Ion Elastic Scattering Processes Using Numerical Model Based on the Partial Wave Parameterised S-Matrix with Regge Pole Factor

R. I. Badran[1] · **I. H. Al-Lehyani**[2]

Received: 20 February 2016 / Published online: 15 April 2016

Abstract Analyses of the angular distributions in the elastic scattering processes of $^{9,\,10,\,11}$Be by the target nucleus ^{64}Zn at the laboratory energies of 27.95 MeV, and $^{4,\,6,\,8}$He by the target nucleus ^{208}Pb at the laboratory energy of 22 MeV are performed. These analyses rely on a numerical model based on a parameterised scattering matrix (S-matrix) derived from Frahn and Venter. They confirm the absence of the Coulomb rainbow peak in angular distributions of elastic scattering in collisions of halo nuclei at energies around the Coulomb barrier. The correlation between the total reaction cross section and the halo structure for each scattering that involves a halo nucleus is discussed, and values of the total reaction cross section are found comparable with those of others. The diffractive features of the systems $^{16,\,18}$O + ^{19}F at specific laboratory energies are examined, and the effect of exchanging the projectile and target nuclei at such energies on these features are inspected. The incorporation of the Regge pole factor into the parameterised S-matrix calculations, which is found important in some cases, is employed in order to account for the oscillatory structure (if available) at backward angles. The theoretical results are found reasonable, reproducing the general pattern of the data. The trend of the extracted parameters meets the requirements proposed by the adopted models.

Keywords Heavy-ion scattering · Elastic scattering · Strong absorption model · Frahn and Venter parameterisation · Regge pole formalism

1 Introduction

Several analytical and numerical approaches became available to analyse experimental elastic angular distributions in heavy ion scattering. These approaches are based on the partial wave expansion in the presence of strong absorption [1–21]. Here, the detailed form of scattering matrix (S-matrix) around the grazing angular momentum can be neatly related to the scattering data. The S-matrix, which represents the effect of the scattering potential on the incident wave, may be determined fitting its angular momentum components to the measured elastic angular distribution. It has been found that the parameterised S-matrix is a source of important information which is needed in calculations of transfer reactions based on the strong absorption model [22–24].

All the scattering amplitudes of nuclear optical potentials (apart from a few exceptions) exhibit prominent Regge poles. These poles manifest themselves as resonance peaks in the ℓ dependence of the S-matrix and were found responsible for the oscillatory structure of the elastic angular distribution at backward angles [6, 19, 25–31]. The experimental angular distributions of elastic scattering exhibit strong oscillatory structure at backward angles, especially for nuclei of mass number ≥40 [32, 33]. According to Austern [33], the destructive interferences in the S-matrix may correspond to the single-particle resonances that occurr in optical model calculations. In this way, the contribution of the nuclear S-matrix to the cross section may be considered as a background and must be multiplied by a single pole factor. The incorporation of a Regge pole at $\ell \approx kR$ to the parameterised cut-off model may lead to reasonable fits of the angular distribution, especially at backward angles [28, 30]. The elastic scattering of alpha particles on ^{16}O was analysed by examining single-particle

✉ R. I. Badran
rbadran@hu.edu.jo; rbadran55@gmail.com

[1] The Hashemite University, P.O. Box 150459, Zarqa, Jordan

[2] King Abdulaziz University, Jeddah, Kingdom of Saudi Arabia

Regge poles similar to those naturally occurring in any optical model calculation by suggesting the multiplication of the background S-matrix by a single Regge pole factor [28]. In an approach, the multiplication of the background S-matrix using Ericson formula by a single Regge pole factor was considered for studying the single-particle Regge poles that affect both the amplitude and phase of the scattering matrix elements [30].

In order to analyse experimental angular distributions in the elastic scattering ^{28}Si + ^{16}O at centre of mass energies between 18.67 and 22.29 MeV in the angular range of centre of mass angles from 0° to 180°, the analytical form of the scattering function of Frahn and Venter was used as background. Then, the Regge pole factor of the scattering matrix was introduced [31]. Furthermore, a phase factor was inserted in the Regge pole factor. This insertion led to a successful estimation of the phase angle of the pole [31]. In this latter approach, seven adjustable parameters were used.

Recent studies were carried out using the optical model (OM) to analyse elastic angular distributions in the scattering of ^{9,10,11}Be from ^{64}Zn, at a laboratory energy of 27.95 MeV [34]. Moreover, both OM and/or coupled reaction channel (CRC) models were employed to analyse elastic scattering and the effect of the stripping of 1n in the ^{4,6,8}He + ^{208}Pb collision, at a laboratory energy of 22 MeV [35–37]. Some of these collisions involve a halo nucleus with energy around the Coulomb barrier. It is well-known that the halo nucleus (which consists of a core nucleus plus one or more weakly bound neutrons) is a loosely bound system. Such nucleus can be easily polarised. This polarisation occurs when the nucleus is submitted to a strong electric field. Then, it becomes distorted such that the positively charged core moves in the direction of the field while the halo neutrons move in the opposite direction (in the centre of mass frame). In an earlier study, the molecular two-state approximation was performed to analyse the angular distributions of the systems ^{19}F + ^{16}O and ^{19}F + ^{18}O at laboratory energies of 27, 30, 33 and 36 MeV and 27, 30 and 33 MeV, respectively, and the systems $^{16,\ 18}$O + ^{19}F at laboratory energies of 30.4 and 31.16 MeV [38]. The same study was extended to the system ^{15}N + ^{19}F at laboratory energies of 23, 26 and 29 MeV [38].

In the present study, the available experimental angular distributions in the elastic scattering of ^{9,10,11}Be from ^{64}Zn at a laboratory energy of 27.95 MeV [34], and $^{4,\ 6,\ 8}$He + ^{208}Pb at a laboratory energy of 22 MeV [35–37] will be analysed, using the strong absorption model of Frahn and Venter (SAM)[1, 18, 19]. The analysis of SAM will explain the diffractive features that occur at forward angles when the projectile has a nuclear halo structure. This may allow us to explore the existence (or not) of a Fresnel-type pattern in the angular distribution at forward angles, investigating the absence of a Coulomb rainbow in such elastic scattering processes. This analysis will also allow the determination of several useful parameters and physical quantities, such as the grazing angular momentum Λ, the width of the ℓ-space window that contributes to elastic scattering, Δ, the nuclear phase shift, μ, the total reaction cross section σ_r, etc. [17–21]. For an attempt to improve the fits and search for possibly existing Regge poles, which may be responsible for structures in the angular distribution, especially at backward angles, the numerical combined model will be employed using seven adjustable parameters (three SAM plus four Regge pole parameters) [17, 31]. The theoretical elastic angular distributions in collisions of different isotopes with the same target and the same laboratory energy are obtained for a full range of centre of mass angles (0–180°), using the combined model. At the first stage, the three parameters extracted from the Frahn and Venter model (FVM) analyses are used as fixed entries for the numerical combined model applied to forward angles. At the second stage, our analyses will be extended to investigate the existence of oscillatory structures in the angular distribution at backward angles. This will be achieved by introducing the Regge pole factor in the scattering matrix elements, following the approach of Mermaz et al., using the parameterised scattering matrix of SAM as background [1, 31]. Thus, the effect of the nuclear halo structure in elastic scattering will also be investigated using the combined model. A similar analysis will be conducted to the systems $^{16,\ 18}$O + ^{19}F at laboratory energies of 30.4 and 31.16 MeV [38]. The diffractive features, from the point of view of SAM, will be inspected and the effect of swapping the projectile and target nuclei on these features will be shown. The available experimental data and the theoretical angular distributions for the systems ^{19}F + ^{16}O and ^{19}F + ^{18}O at laboratory energies of 27, 30, 33 and 36 MeV and 27, 30 and 33 MeV, respectively, will be compared to each other and to the systems $^{16,\ 18}$O + ^{19}F. Furthermore, on the basis of the strong absorption model, the study is extended to the system ^{15}N + ^{19}F at laboratory energies of 23, 26 and 29 MeV and comparison to the previous systems is made. Moreover, the position and phase angle of the pole will be obtained and the amplitude and width of the resonance can be estimated when using the combined model. The behaviour of the extracted parameters due to the change in the size of the projectile and/or target nucleus and incident energy will be investigated.

2 Theoretical Models

2.1 Frahn and Venter Model

The scattering amplitude of heavy-ion elastic scattering is the sum of the nuclear and Coulomb scattering amplitudes. In the scattering amplitude of partial wave analysis of heavy-ion elastic scattering, the nuclear scattering amplitude is given by:

$$f_{\mathrm{N}}(\theta) = (2ik)^{-1}\sum_{\ell=0}^{\infty} (2\ell+1)e^{2i\sigma_\ell}\left[S_{\ell,\mathrm{N}}-1\right]P_\ell(\cos\theta) \tag{1}$$

Here, k, σ_ℓ and $P_\ell(\cos\theta)$ are the wave number, Coulomb phase shifts and Legendre polynomials, respectively. The nuclear scattering matrix element $S_{\ell,\mathrm{N}} = \eta_\ell e^{2i\delta_{\ell,\mathrm{N}}}$ where η_ℓ is called the reflection coefficient and $\delta_{\ell,\mathrm{N}}$ is the real part of the phase shifts due to elastic scattering. Furthermore, the concept of nuclear phase shifts $\delta_{\ell,\mathrm{N}}$ is introduced into the partial wave to account for the effect of nuclear potential in the nuclear scattering.

In the Frahn-Venter model, the scattering matrix elements $S_{\ell,\mathrm{N}}$, in Eq. 1, become a continuous function $S(\lambda)$ of the angular momentum λ where the summation over ℓ in the partial wave expansion can be replaced by integration over λ. Moreover, the grazing angular momentum value of λ becomes Λ. The continuous function, however, is expressed by [1]:

$$S(\lambda) = S_{\mathrm{N}}(\lambda)e^{2i\sigma(\lambda)} \tag{2}$$

Where

$$S_{\mathrm{N}}(\lambda) = \eta(\lambda)e^{2i\delta_{\mathrm{N}}(\lambda)} \tag{3}$$

The reflection coefficient function $\eta(\lambda)$ is rapidly varying between near-zero to unity over the transition region centred on the grazing angular momentum Λ [1]. In angular momentum space (ℓ-space), it was found that the derivative of reflection coefficient function $\eta(\lambda)$ is localised within a narrow window of width Δ around $\lambda = \Lambda$. Frahn and Venter showed, in an analytical approach, that the derivative of $S_{\mathrm{N}}(\lambda)$ with respect to λ has a major role in understanding the nuclear interaction [1]. However, the nuclear interaction could be represented by Fourier transform of the latter derivative of function. In this way, it was realised that the scattering function with such properties lends the analytical formalism of normal strong absorption features. Therefore, the nuclear interaction function may be written as [18]

$$D_{\mathrm{N}}(\lambda) = \left[\frac{\mathrm{d}\eta(\lambda)}{\mathrm{d}\lambda} + i\eta(\lambda)\theta_{\mathrm{N}}(\lambda)\right]e^{i2\delta_{\mathrm{N}}(\lambda)} \tag{4}$$

In such case, the total quantal function constitutes of quantal Coulomb θ_{R} (λ) and nuclear θ_{N} (λ) functions where the latter was clearly introduced by this model. In particular, the total quantal deflection function is written as the sum of θ_{R} (λ) and θ_{N} (λ), namely [18]:

$$\theta(\lambda) = \theta_{\mathrm{N}}(\lambda) + \theta_{\mathrm{R}}(\lambda), \tag{5}$$

where,

$$\theta_{\mathrm{N}}(\lambda) = -\frac{2\mu}{\Delta}\frac{e^{\frac{(\lambda-\Lambda)}{\Delta}}}{\left[1+e^{\frac{(\lambda-\Lambda)}{\Delta}}\right]^2} \tag{6}$$

and

$$\theta_{\mathrm{R}}(\lambda) = \frac{2\mathrm{d}\sigma(\lambda)}{\mathrm{d}\lambda} = 2\tan^{-1}\left(\frac{n}{\Lambda}\right) \tag{7}$$

However, $\theta_{\mathrm{R}}(\lambda)$ was found from the derivation of the Coulomb phase shifts (i.e. $\sigma_\lambda = \arg\Gamma(\lambda+1+in)$) which are given by the exact solution of the Rutherford scattering problem. The Sommerfeld parameter, n, represents the strength of Coulomb interaction.

The scattering amplitude, $f(\theta) = f^+(\theta) + f^-(\theta)$, as given by the Frahn-Venter approach [1], is composed of two components: the component $f^+(\theta)$ consists of the Rutherford scattering amplitude $f_{\mathrm{R}}(\theta)$ plus a nuclear amplitude part which depends on the Fourier transform of the absorptive shape function $D_{\mathrm{N}}(\lambda) = \frac{\mathrm{d}S_{\mathrm{N}}(\lambda)}{\mathrm{d}\lambda}$. In particular, the nuclear scattering amplitude depends on the function $F[(\Delta(\theta_{\mathrm{R}} - \theta)]$, namely [17]:

$$F[\Delta(\theta_{\mathrm{R}}-\theta)] = \int_{-\infty}^{\infty} D_{\mathrm{N}}(\lambda)e^{-i(\lambda-\Delta)\big/t}\,\mathrm{d}\lambda, \tag{8}$$

where $t = \theta - \theta_{\mathrm{R}}$.

Based on the diffraction model (or SAM), the nature of the diffraction pattern is governed by the interference of the two components of the scattering amplitude in the interaction region of two colliding nuclei. In the near side of the interaction region (called illuminated region at $\theta \le \theta_{\mathrm{R}}$), the component of scattering amplitude consists of the Rutherford scattering amplitude represented by the Coulomb trajectory and a nuclear amplitude part, which depends on the Fourier transform of the absorptive shape function $D_{\mathrm{N}}(\lambda)$, represented by the grazing trajectory. The Fresnel diffraction nature of the scattering is embodied by the modification of Coulomb scattering by the nuclear amplitude part. However, the far-side branch of the scattering amplitude in a region called the shadow region (at $\theta \ge \theta_{\mathrm{R}}$) is purely diffractive and is represented by the nuclear part only. The Fraunhofer diffraction nature of the scattering is embodied by the nuclear part only [1, 17–19]. Thus, the interference between these two components may result in Fresnel oscillation pattern. However, in the shadow region ($\theta \ge \theta_{\mathrm{R}}$), the Coulomb trajectories are absorbed and the amplitude is resulted from the interference of near-side and far-side diffracted waves. This gives the Fraunhofer oscillation structure. The "far-side" branch also depends on the Fourier transform of $D_N(\lambda)$ but with $t = \theta - \theta_R$ (see Eq. 7). This may be represented by a diffracted wave with grazing trajectory on the "far-side" of the nucleus.

In this study, however, the Woods-Saxon type of reflection coefficient is employed [1]. Here, Λ and Δ from the reflection coefficient relation together with the parameter μ which represents the refractive strength of the nuclear interaction will be the adjustable parameters for FVM calculations.

The interaction radius and the diffusivity are given, here, by [1, 17–19]:

$$R = \frac{1}{k}\left[n + \left(\Lambda^2 + n^2\right)^{1/2}\right] \tag{9}$$

$$d = \frac{\Delta}{k\sqrt{1 + \left(n/\Lambda\right)^2}} \tag{10}$$

However, the type of diffraction pattern from a target nucleus in an elastic scattering is characterised by "pattern parameter" $p = \frac{2n}{1+(n/\Lambda)^2}$. It is expected that a diffractive Fresnel type dominates the angular distribution of elastic scattering for most heavy ions when $p > 1$. Here, the value of p is obviously determined by both Sommerfeld parameter n and the grazing angular momentum parameter Λ.

If both the Coulomb parameter n and h (the ratio of the centre of mass kinetic energy $E_{\mathrm{c.m.}}$ to the Coulomb barrier V_C) are known, then a simple classification to all scattering processes of charged particles above the Coulomb barrier [4] may be identified. Here, h can also be expressed as

$$h = \frac{1}{2}\left(1 + \csc\frac{\theta_R}{2}\right), \tag{11}$$

As mentioned above, SAM provides us with the characteristic qualitative features that are usually observed in the experimental data of angular distribution of elastic scattering. The S-matrix, in this sense, becomes a tool for studying the surface properties of the scattering of charged particles. If any pair of the parameters (Λ, p) or (h, n), for example, for $^{16}\mathrm{O} + ^{208}\mathrm{Pb}$ elastic scattering at laboratory energy of 157 MeV, which were found to be the same as those of $^{19}\mathrm{F} + ^{159}\mathrm{Tb}$ elastic scattering at laboratory energy of 142 MeV [8], then these two different reactions are represented by the same point on the diffraction diagram. The angular distributions of these two different reactions are called "homomorphic" [8].

The total reaction cross section from the generalised Fresnel model (GFM) is expressed as [5, 19]:

$$\sigma_r = \frac{\pi\Lambda^2}{k^2}\left[1 + \frac{2\Delta}{\Lambda} + \frac{1}{3}\left(\frac{\pi\Delta}{\Lambda}\right)^2\right] \tag{12}$$

From the simple Fresnel model (FM), σ_r, is given by [5, 19]:

$$\sigma_r = \frac{\pi}{k^2}(\Lambda + 1)^2 \tag{13}$$

2.2 Regge Pole Model (RPM) and the Modified S-Matrix

The modified scattering matrix was formed when the Regge pole factor is added to the S-matrix of Frahn-Venter [31]. Moreover, a phase factor of $e^{i\varphi_{\lambda\circ}}$ was also introduced for the Regge pole. This modified model is adopted here where a combination of the three parameters of FVM and the four parameters of Regge pole model will be employed as adjustable parameters. The modified S-matrix, which constitutes the Frahn-Venter parameterised form (S_λ^{FV}) as the background S-matrix and the Regge pole factor, is expressed by [19, 31]:

$$S(\lambda) = S_\lambda^{\mathrm{FV}} + \frac{iD(\lambda)e^{\lambda\phi_{\lambda o}}}{\lambda - \lambda_o - i\Gamma(\lambda)/2}, \tag{14}$$

where the amplitude of the pole is

$$D(\lambda) = D_o\left[1 - \mathrm{Re}S_\lambda^{\mathrm{FV}}\right], \tag{15}$$

and the width of the pole is

$$\Gamma(\lambda) = \Gamma_\circ\left[1 - \mathrm{Re}S_\lambda^{\mathrm{FV}}\right] \tag{16}$$

The real part of S_λ^{FV} is expressed elsewhere [1, 6, 18].

Both quantities in square brackets of Eqs. 15 and 16 represent damping functions which play an important role in avoiding unwanted oscillations of the angular distribution caused by high orbital angular momentum [31]. Here, $D_\circ$ and $\Gamma_\circ$ represent reduced amplitude and reduced width, respectively [31]. The location of the pole $\lambda_\circ$ and its phase $\varphi_{\lambda\circ}$ together with and $\Gamma_\circ$ will be used as free parameters in the numerical combined model. The numerical combined model of both FVM and Regge is developed to reproduce the cross sections of elastic scattering at two ranges of the centre of mass angles (i.e. forward and backward angles). This is because the parameterised model of FV cannot successfully reproduce, by itself, the cross sections at backward angles, especially for the systems that contain deep oscillations in their angular distribution.

3 Results and Discussion

Using our developed FORTRAN codes, the theoretical results of the ratio of elastic scattering cross section to Rutherford cross section for a set of elastic scattering reactions at different angles and energies are obtained by adopting both FVM and the combined model. The quality of the best fit to the experimental data of angular distribution of elastic scattering is judged visually and by the χ^2 indicator. Moreover, each of the adjustable parameters (Λ, Δ and μ) for FVM and $D_\circ$, $\Gamma_\circ$, $\lambda_\circ$ and $\varphi_{\lambda_\circ}$ for the Regge pole model is introduced with an initial value and is carefully changed in very small steps and the best fit to experiment is reached when χ^2 is minimised. The average value of 10 % of the experimental data is considered for each experimental error at certain energy of an elastic scattering.

3.1 Elastic Scattering of $^{9,\ 10,\ 11}$Be by Target Nucleus ^{64}Zn

Figure 1 presents the experimental angular distribution of the elastic scattering $^{9,\ 10,\ 11}$Be + ^{64}Zn at a laboratory energy of 27.95 MeV [34]. The theoretical results of the angular distribution have been obtained using FV and combined models. Three adjustable parameters are used to reproduce the cross sections for the whole given range of angles when employing FVM only. The reproduced results are reasonably fitted to experimental data at incident energy of 27.95 MeV, as shown in Fig. 1.

The angular distribution of the elastic scattering process (as shown in Fig. 1), which has ^{9}Be projectile, exhibits similar diffraction features to that involving the ^{10}Be projectile. In particular, both experimental data and theoretical results of angular distribution for ^{9}Be and ^{10}Be projectiles demonstrate typical Fresnel diffraction patterns and cross section fall-off while that for the ^{11}Be projectile shows extremely different behaviour [34]. For the ^{11}Be projectile, the Fresnel diffraction oscillation peak does not exist and the Coulomb amplitude exhibits damping at forward angles lower than the grazing angle. This was attributed to the long range absorptive surface potential. It was found that the reduction in the cross section occurred at lower forward angles or larger partial waves. This latter reduction was ascribed to the diffuse nuclear halo structure of ^{11}Be [34]. It was also found that a better quality fitting to experimental data might be reached, when a surface term was added to the imaginary term of the potential when adopting OM [34]. Although the inclusion of dynamic polarisation potentials in the optical model analysis produced a strong reduction of elastic cross section in the Coulomb-nuclear interference region, this is not enough to reproduce the experimental data of angular distribution. This is because couplings to other non-elastic channels are also possible and must be included in the calculations. Here, we found that the total classical deflection function does not exhibit any maximum around the grazing angular momentum. This, however, asserts the absence of any possible Coulomb rainbow for the ^{11}Be + ^{64}Zn system. Our analysis shows that a higher value of diffusivity ($\Delta = 3.61$) is obtained for the projectile ^{11}Be than those of the two isotopes of ^{9}Be and ^{10}Be ($\Delta = 3.23$) and ($\Delta = 3.54$), respectively. Such results also indicate that the diffusivity in the interaction nuclear region of the two colliding nuclei depends on the projectile properties and not only on the target. This is in agreement with the analysis of the optical potential model used by other groups [34, 38]. It was believed that the large diffusivity may be related to the decay length of the halo neutron initial state wave function and may be found necessary to reproduce the behaviour of the elastic cross section at the Coulomb-nuclear interference peak. Moreover, our

Fig. 1 **a**–**c** The experimental data (*symbols*) of angular distribution of elastic scattering of $^{9,\ 10,\ 11}$Be by the target nucleus ^{64}Zn at laboratory energies of 27.95 MeV are shown and compared to the theoretical results obtained using FVM only (*dashed line*) and the combined model of Frahn-Venter and Regge (*solid line*)

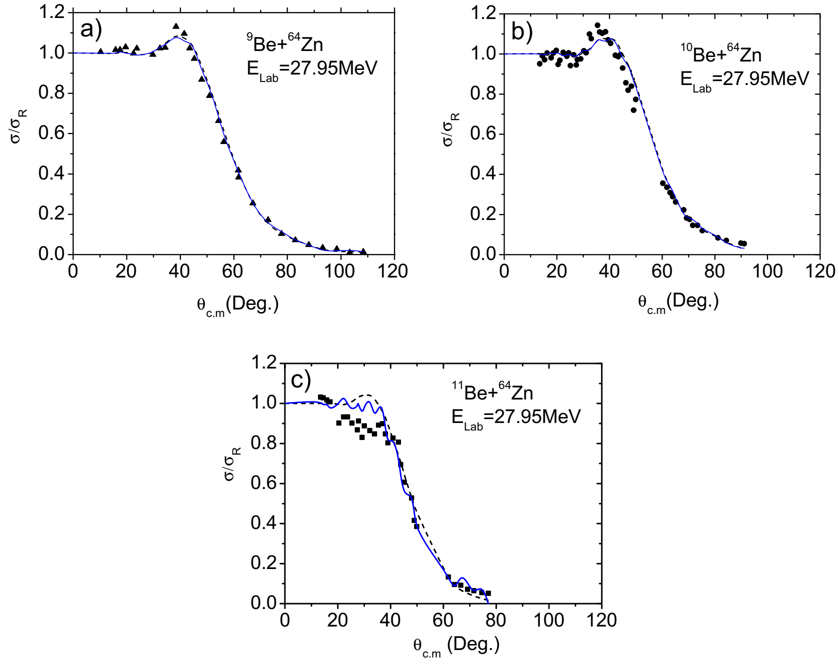

results show a higher value of total reaction cross section, as obtained from both GFM and FM, in the halo nucleus case of the ^{11}Be projectile than the corresponding ones in other cases of ^{9}Be and ^{10}Be projectiles. These results are also in agreement with those of other groups [34]. Here, the Regge pole analysis does not prominently contribute to any significant improvement in the results. This is because the experimental data do not exhibit strong oscillatory behaviour at backward angles. Thus, the reproduction of cross sections in the whole angular rang using SAM is quite satisfactory (Table 1).

3.2 Elastic Scattering of $^{4,\,6,\,8}$He by Target Nucleus ^{208}Pb

Figure 2 shows the experimental data of angular distribution of elastic scattering for $^{4,\,6,\,8}$He + ^{208}Pb elastic scattering at laboratory energy of 22 MeV [35–37] together with the calculated results of angular distribution using FVM and the combined model. The theoretical results of our adopted models are consistent with experimental data for ^{4}He [36, 37]. Furthermore, the total deflection function (Eq. 5) is tested for a possible presence of rainbow, and the results confirm the absence of any rainbow in the three elastic scatterings of $^{4,\,6,\,8}$He + ^{208}Pb. The list of extracted parameters is seen in Table 2.

Our analysis shows that the values of diffusivity parameter Δ and grazing angular momentum Λ for the three scattering cases $^{4,\,6,\,8}$He + ^{208}Pb at the same incident energy (22 MeV) are increasing with the increase in atomic mass from 4 to 8. The quarter point angle $\theta_{1/4}$ values are not quite comparable to θ_R. The value of the total reaction cross section obtained for ^{8}He + ^{208}Pb system is larger than that of ^{6}He + ^{208}Pb and ^{4}He + ^{208}Pb. This is again attributed to nuclear halo properties,

Table 1 List of parameters for elastic scattering of $^{9,\,10,\,11}$Be by the target nucleus ^{64}Zn at laboratory energies of 27.95 MeV, which are extracted from the analyses using both FVM only and the combined model. The total reaction cross sections σ_r (FM) and σ_r (GFM) are obtained from the Fresnel model (FM) and the generalised Fresnel model (GFM), respectively

Elastic scattering		^{9}Be + ^{64}Zn	^{10}Be + ^{64}Zn	^{11}Be + ^{64}Zn
$E_{\mathrm{Lab.}}$ (MeV)		27.95	27.95	27.945
Λ	[FVM]	14	15	22
	[Combined]	14	15	22
Δ	[FVM]	3.23	3.54	3.61
	[Combined]	3.23	3.54	3.61
$\frac{\mu}{2\Delta}$ (Rad)	[FVM]	0.67	0.68	0.15
	[Combined]	0.67	0.68	0.15
r_o (fm)	[FVM]	1.55	1.56	1.85
	[Combined]	1.55	1.56	1.85
d (fm)	[FVM]	0.85	0.9	0.98
	[Combined]	0.85	0.9	0.98
$\lambda_\circ$		9.05	12.04	27.53
$\varphi_{\lambda_\circ}$ (deg)		29.1	35.1	57.159
$D_\circ$		2.22	3.22	109.3
$\Gamma_\circ$		1.48	1.7	91.76
R (fm)	[FVM]	9.42	9.6	11.51
	[Combined]	9.42	9.6	11.51
d/R	[FVM]	0.09	0.094	0.085
	[Combined]	0.09	0.094	0.085
p	[FVM]	13.52	14.42	18.38
n	[FVM]	10.73	11.31	11.858
h	[FVM]	1.336	1.34	1.588
θ_R (Rad)	[FVM]	1.307	1.29	1.116
$\theta_{1/4}$ (Rad)	[Expt.]	1.173	1.16	0.998
θ_{Nucl}[a] (Rad)	[FVM]	−0.104	−0.096	−0.021
σ_r (mb)	[GFM]	1089	1168.7	2011
	[FM]	764.03	804	1551.4
χ^2	[FVM]	2.43	1.23	4.62
	[Combined]	0.0006	0.002	0.005

[a] The value of θ_{Nucl} is obtained when $\lambda = \Lambda$ is substituted into the formula of θ_N (λ) [17]

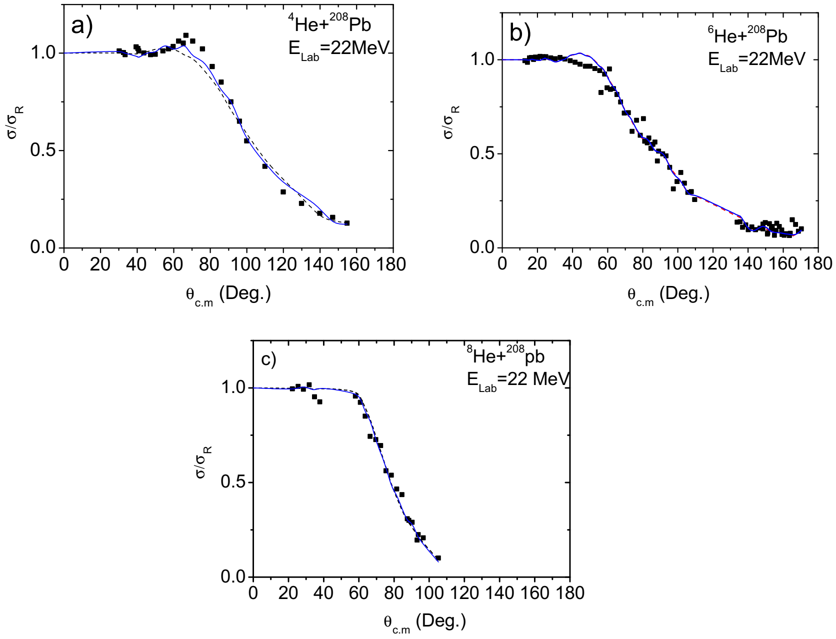

Fig. 2 **a–c** Same as in Fig. 1 but for $^{4,\,6,\,8}$He + ^{208}Pb elastic scattering at laboratory energy of 22 MeV

as mentioned earlier in Subsection 3.1. Here, our values of the interaction radii, as obtained from Eq. 8, are $R = 11.9$ and 13.08 fm for ^{6}He + ^{208}Pb and ^{8}He + ^{208}Pb systems, respectively, which almost agree with those found by others [36]. However, for ^{6}He + ^{208}Pb system, it was found that there is still a significant reduction of the cross sections with respect to the Rutherford values that occurred at much larger distances, up to 20 fm, when the optical model was adopted [36]. It was also shown in ref. [36] that this is a clear indication of the presence of reaction mechanisms that remove flux from the elastic channel in situations for which the nuclei stay well separated. This phenomenon was associated with the scattering of weakly bound nuclei and it was called long range absorption, where the latter is attributed to the combined effects of Coulomb and nuclear couplings to the continuum. It was also concluded that the absence of the rainbow in the case of ^{6}He might be related to greater absorption for $\lambda > \Lambda$ due to the tail (halo) of the ^{6}He density distribution [36]. Thus, it was shown that the large dipole polarisability of the halo nucleus in the Coulomb field of heavy target nucleus (in case of ^{6}He + ^{208}Pb system) led to the reasonable reduction of the cross section. Dipole excitation to the continuum was found to be the dominant effect on this system [39]. Our results reveal that the angular distribution of ^{8}He + ^{208}Pb system has almost similar behaviour to that of ^{6}He + ^{208}Pb system at $\theta < \theta_R$ (apart from a small Coulomb peak located at $\theta_{c.m.} = 45°$) which represent a typical Fresnel pattern, while the fall-off exhibits almost a similar slope for the envelope of angular distribution of both systems, related to the values of Δ ~4.05 and ~4.01, respectively. The observed data of angular distribution of both elastic scatterings of ^{8}He and ^{6}He exhibit a similar trend up to the grazing angle. A larger reduction in cross section for the angular distribution of elastic scattering of ^{8}He at larger angles is also noticed [35]. Regarding the reduction in cross section, the information that really matters is as follows: (1) ^{8}He and ^{6}He have 1*n* and 2*n* systems with similar binding energies, (2) the skin nucleus ^{8}He has a tighter neutron layer than the $\alpha + 2n$ system (or ^{6}He) and (3) the break-up of $\alpha + 2n$ system (in case of ^{6}He) is energetically favourable. Accordingly, it is worth considering the following in any adopted model: Firstly, the effect of tight neutron skin for ^{8}He (which is similar to that of a heavy-ion stable nucleus) is important, although this skin is larger than that of the weakly 2*n*-halo in ^{6}He and a reasonable part of the Coulomb-nuclear peak is suppressed. Secondly, the dominant effect of the competing couplings of the break-up process and the 1*n* stripping process (which seems to be more favourable for ^{8}He than ^{6}He) must be included. Finally, it is worth determining the contribution of both Coulomb and the nuclear couplings to the break-up cross section and the corresponding combined effect on shaping up the elastic angular distribution. Here, in this work, although the fittings to experimental data are quite good, our simple adopted model is not able to resolve the above-mentioned issues.

In our analysis, using the combined model, the Regge pole effect does not show any significant role and the obtained Regge pole parameters did not exhibit any systematic trend upon the change in the mass of the projectile.

In summary, the angular distribution of the elastic scattering of the halo nuclei on targets with medium or heavy masses at low incident energies exhibits a common feature that manifests itself by a reduction of the Coulomb-nuclear interference peak. This reduction in a halo-induced elastic scattering,

Table 2 Same as in Table 1 but for elastic scattering of $^{4,\,6,\,8}$He by the target nucleus ^{208}Pb at laboratory energy of 22 MeV

Elastic scattering		^{4}He + ^{208}Pb	^{6}He + ^{208}Pb	^{8}He + ^{208}Pb
$E_{\mathrm{Lab.}}$ (MeV)		22	22	22
Λ	[FVM]	5	7	14
	[Combined]	5	7	14
Δ	[FVM]	2.61	4.01	4.05
	[Combined]	2.61	4.01	4.09
$\frac{\mu}{2\Delta}$ (Rad)	[FVM]	0.51	0.43	0.44
	[Combined]	0.51	0.43	0.44
r_o (fm)	[FVM]	1.55	1.54	1.65
	[Combined]	1.55	1.54	1.65
d (fm)	[FVM]	0.6	0.83	0.97
	[Combined]	0.6	0.83	0.98
$\lambda_\circ$		13.74	14.65	16.5
$\varphi_{\lambda_\circ}$ (deg)		28.25	51.72	64.9
$D_\circ$		1.2	1.5	1.5
$\Gamma_\circ$		2.5	17.86	8.13
R (fm)	[FVM]	11.644	11.923	13.076
	[Combined]	11.644	11.923	13.076
d/R	[FVM]	0.052	0.07	0.074
	[Combined]	0.052	0.07	0.075
p	[FVM]	2.61	5.72	13.92
n	[FVM]	11.015	13.49	15.577
h	[FVM]	1.064	1.07	1.173
θ_{R} (Rad)	[FVM]	2.28	2.18	1.677
$\theta_{1/4}$ (Rad)	[Expt.]	1.6	2.04	2.26
$\theta_{\mathrm{Nucl}}{}^{\mathrm{a}}$ (Rad)	[FVM]	−0.097	−0.0536	−0.054
σ_r (mb)	[GFM]	569.6	831.9	1461.2
	[FM]	278.9	336.9	905
χ^2	[FVM]	1.55	8.99	0.54
	[Combined]	0.0012	0.0088	0.0014

which is attributed to long range absorption and seems to smooth the surface-leap of the scattering matrix, may lead to a larger total cross section than the corresponding non-halo isotope elastic scattering [34, 40]. Moreover, the effect of Coulomb dipole polarisability was found accountable for the significant part of reduction of cross sections in elastic scattering of halo nuclei on heavy-ion targets.

3.3 Elastic Scattering of $^{16,\,18}$O and ^{15}N by Target Nucleus ^{19}F

The experimental data of angular distribution of ^{15}N + ^{19}F, ^{16}O + ^{19}F and ^{18}O + ^{19}F systems at laboratory energies of 26, 30.4 and 31.16 MeV, respectively, are shown in Fig. 3 [41]. Our theoretical results show fair agreement with the experimental data when FVM is used. A mild improvement in the fits occurs when the combined model is employed especially at backward angles where the reproduction of the experimental data is successful. In most of our attempts to get the best fit using the combined model, the three parameters obtained from FVM are kept fixed, but with some exceptions. The Regge pole parameters $\lambda_\circ$, $\varphi_{\lambda_\circ}$, $D_\circ$ and $\Gamma_\circ$ are found

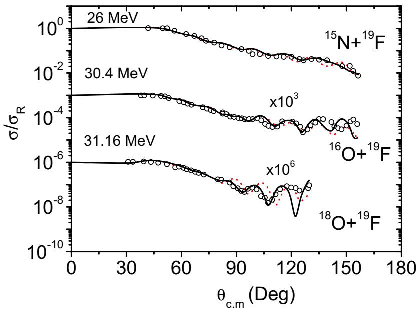

Fig. 3 Same as in Fig. 1 but for elastic scattering of ^{15}N + ^{19}F, ^{16}O + ^{19}F, and ^{18}O + ^{19}F at laboratory energies of 26, 30.4 and 31.16 MeV, respectively

Table 3 Same as in Table 1 but for elastic scattering of $^{15}N+^{19}F$, $^{18}O+^{19}F$ and $^{16}O+^{19}F$ at laboratory energies of 26, 30.4 and 31.16 MeV, respectively

Elastic scattering		$^{15}N+^{19}F$	$^{16}O+^{19}F$	$^{18}O+^{19}F$
$E_{\text{Lab.}}$ (MeV)		26	30.4	31.16
Λ	[FVM]	10	11	11
	[Combined]	10	11	10
Δ	[FVM]	0.33	0.224	0.067
	[Combined]	0.33	0.224	0.34
$\frac{\mu}{2\Delta}$ (Rad)	[FVM]	0.5	0.5	1.2
	[Combined]	0.5	0.4	1.35
r_o (fm)	[FVM]	1.65	1.66	1.61
	[Combined]	1.65	1.66	1.6
d (fm)	[FVM]	0.112	0.07	0.02
	[Combined]	0.112	0.07	0.1
$\lambda_\circ$		7.3	15.16	11.35
$\varphi_{\lambda_\circ}$ (deg)		33.84	69.89	68.5
$D_\circ$		11.18	17.7	4.3
$\Gamma_\circ$		9.44	7.636	2.85
R (fm)	[FVM]	8.47	8.61	8.515
	[Combined]	8.47	8.61	8.5
d/R	[FVM]	0.013	0.0081	0.00235
	[Combined]	0.013	0.0081	0.012
p	[FVM]	9.62	10.55	10.68
n	[FVM]	7.54	8.23	8.62
h	[FVM]	1.35	1.371	1.3
θ_R (Rad)	[FVM]	1.29	1.28	1.32
$\theta_{1/4}$ (Rad)	[Expt.]	1.34	1.297	1.26
$\theta_{\text{Nucl}}{}^a$ (Rad)	[FVM]	−0.75	−1.12	−8.9
σ_r (mb)	[GFM]	577.7	577.08	543.85
	[FM]	653.5	659.57	639.14
χ^2	[FVM]	18.198	15.13	122.9
	[Combined]	0.00176	0.00372	0.0066

responsible for improving the reproduction of the oscillations at backward angles but do not follow any specific trend when both the size of the projectile and incident energy change, as seen in Table 3. Both $\lambda_\circ$ and $\varphi_{\lambda_\circ}$ are more sensitive than $D_\circ$ and $\Gamma_\circ$ in changing the size and number of oscillations at backward angles. Here, the theoretical results also show that the values of grazing angular momentum Λ (or r_o) increases and diffusivity, Δ, in ℓ-space decreases with the increase in both the mass of the projectile and laboratory energy, as expected from SAM prescription (see Table 3). However, the increase in the value of μ may be attributed to the increase in the oscillatory structure in the shadow region with increasing incident energy and size of the projectile nucleus. The approximation $\theta_R \approx \theta_{1/4}$ also holds and this is in agreement with the prediction of SAM. It has been noticed that the value of the ratio d/R decreases when the both the mass of the projectile and incident energy increase. Furthermore, as predicted from both GFM and FM, the change in the values of the total cross sections for the three systems is not very tangible

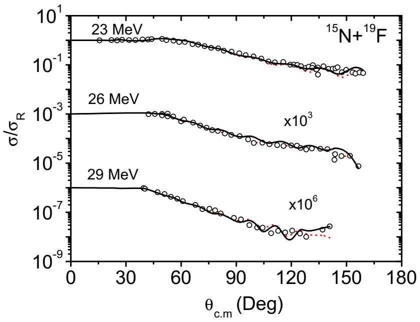

Fig. 4 Same as in Fig. 1 but for $^{15}N+^{19}F$ elastic scattering at laboratory energies of 23, 26 and 29 MeV

Table 4 Same as in Table 1 but for ^{15}N + ^{19}F elastic scattering at laboratory energies of 23, 26 and 29 MeV

Elastic scattering		^{15}N + ^{19}F		
$E_{\text{Lab.}}$ (MeV)		23	26	29
Λ	[FVM]	7	10	12
	[Combined]	7	10	12
Δ	[FVM]	0324	0.33	0.424
	[Combined]	0.324	0.33	0.44
$\frac{\mu}{2\Delta}$ (Rad)	[FVM]	0.48	0.5	0.6
	[Combined]	0.48	0.5	0.61
r_o (fm)	[FVM]	1.65	1.65	1.66
	[Combined]	1.65	1.65	1.66
d (fm)	[FVM]	0.1	0.112	0.145
	[Combined]	0.1	0.112	0.15
$\lambda_\circ$		9.56	7.3	10.56
$\varphi_{\lambda_\circ}$ (deg)		45.1	33.84	54.89
$D_\circ$		15.1	11.18	14.76
$\Gamma_\circ$		7.7	9.44	6.21
R (fm)	[FVM]	8.472	8.47	8.523
	[Combined]	8.472	8.47	8.523
d/R	[FVM]	0.012	0.013	0.017
	[Combined]	0.012	0.013	0.0176
p	[FVM]	6.94	9.62	10.54
n	[FVM]	8.014	7.54	7.14
h	[FVM]	1.2	1.35	1.52
θ_{R} (Rad)	[FVM]	1.7	1.29	1.073
$\theta_{1/4}$ (Rad)	[Expt.]	1.69	1.34	1.145
$\theta_{\text{Nucl}}{}^{\text{a}}$ (Rad)	[FVM]	−0.74	−0.75	−0.708
σ_{r} (mb)	[GFM]	328.21	577.7	747.74
	[FM]	389.94	653.5	816.65
χ^2	[FVM]	9.24	18.198	20.47
	[Combined]	0.0098	0.00176	0.00076

(see Table 3). Both the experimental data and our results demonstrate that the number of oscillations in the angular distribution of the three systems under study is almost the same. Due to SAM, the latter argument may be justified by obtaining almost similar values of the pair (n, h) for the three systems. This, however, refers to the fact that such systems may be homomorphic. This also indicates that the description of the strong absorption elastic scattering process using parameterised models is model independent.

The fit to the experimental data of the angular distribution of elastic scattering ^{15}N + ^{19}F at different incident laboratory energies of 23, 26 and 29 MeV [41] is conducted using FVM and the results are presented in Fig. 4, where the extracted parameters can be seen in Table 4. The behaviour of adjustable parameters Λ (or r_o), Δ and μ is as expected and predicted by SAM. The theoretical results obtained from the combined model show good fit to the experimental data. The seven adjustable parameters of both the Regge pole and FVM are listed in Table 4. The experimental data is well-reproduced when the combined model is employed (see Fig. 4). The three adjustable parameters of FVM obtained earlier are used as fixed entries in the numerical combined model. However, the four Regge pole parameters $\lambda_\circ$, $\varphi_{\lambda_\circ}$, Γ_o and D_o are

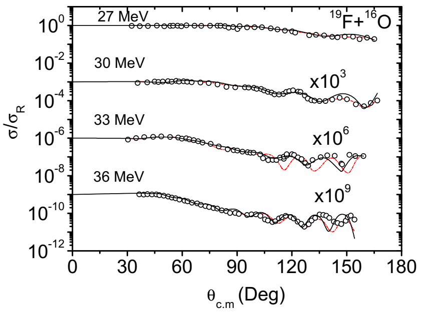

Fig. 5 Same as in Fig. 1 but for ^{19}F + ^{16}O elastic scattering at laboratory energies of 27, 30, 33 and 36 MeV

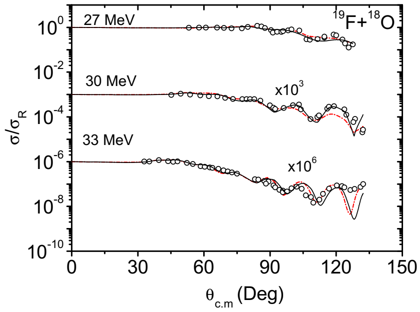

Fig. 6 Same as in Fig. 1 but for $^{19}F+^{18}O$ elastic scattering at laboratory energies of 27, 30 and 33 MeV

adjusted until the best fit is reached and χ^2 is minimised. This reveals the existence of poles which are responsible for affecting the location of the deepest minimum of the oscillatory structure back and forth along the angular range. The parameter $\varphi_{\lambda_\circ}$ is found, in particular, controlling the size of oscillation at backward angles.

3.4 Elastic Scattering of ^{19}F by Target Nuclei $^{16,\,18}O$

Figure 5 shows the experimental data of angular distribution for elastic scattering $^{19}F+^{18}O$ at laboratory energies of 27, 30 and 33 MeV [41]. The experimental data of angular distribution for elastic scattering $^{19}F+^{16}O$ at laboratory energies of 27, 30, 33 and 36 MeV is shown in Fig. 6 [41]. The corresponding theoretical results using both FVM and the combined model are also shown in Figs. 5 and 6. All obtained parameters and physical quantities together with the values of χ^2 from both models are listed in Tables 5 and 6.

The reproduced results are reasonably fitted to experimental data for the forward angles at all incident energies for the two processes. Pronounced deviation of theoretical results from experimental data at backward angles does exist, where FVM is found unable to reproduce exactly the size and location of experimental oscillations with reasonable success.

Table 5 Same as in Table 1 but for $^{19}F+^{16}O$ elastic scattering at laboratory energies of 27, 30, 33 and 36 MeV

Elastic scattering		$^{19}F+^{16}O$			
$E_{\text{Lab.}}$ (MeV)		27	30	33	36
Λ	[FVM]	2	6	9	11
	[Combined]	2	6	9	11
Δ	[FVM]	0.295	0.312	0.33	0.33
	[Combined]	0.295	0.312	0.33	0.33
$\frac{\mu}{2\Delta}$ (Rad)	[FVM]	0.35	0.37	0.6	0.6
	[Combined]	0.35	0.37	0.4	0.6
r_o (fm)	[FVM]	1.65	1.65	1.66	1.67
	[Combined]	1.65	1.65	1.65	1.67
d (fm)	[FVM]	0.035	0.08	0.099	0.103
	[Combined]	0.035	0.08	0.099	0.103
$\lambda_\circ$		7.05	4.45	10.56	10.58
$\varphi_{\lambda_\circ}$ (deg)		43.97	55.4	28.0	95.2
$D_\circ$		15.55	14.8	12.3	17.8
$\Gamma_\circ$		4.77	7.2	2.77	9.9
R (fm)	[FVM]	8.56	8.56	8.61	8.66
	[Combined]	8.56	8.56	8.56	8.66
d/R	[FVM]	0.0041	0.0093	0.011	0.012
	[Combined]	0.0041	0.0093	0.012	0.012
p	[FVM]	0.805	5.53	8.99	10.556
n	[FVM]	9.513	9.025	8.605	8.24
h	[FVM]	1.02	1.13	1.253	1.37
θ_R (Rad)	[FVM]	2.73	1.97	1.524	1.286
$\theta_{1/4}$ (Rad)	[Expt.]	2.54	2.01	1.534	1.3
θ_{Nucl}[a] (Rad)	[FVM]	−0.59	−0.593	−0.905	−0.914
σ_r (mb)	[GFM]	33.46	221	437.33	588.6
	[FM]	55.1	270.03	500.9	661.3
χ^2	[FVM]	19.9	4.72	16.854	15.6
	[Combined]	0.057	0.0093	0.0028	0.0046

Table 6 Same as in Table 1 but for ^{19}F + ^{18}O elastic scattering at laboratory energies of 27, 30 and 33 MeV

Elastic scattering		^{19}F + ^{18}O		
$E_{\text{Lab.}}$ (MeV)		27	30	33
Λ	[FVM]	5	8	11
	[Combined]	5	8	11
Δ	[FVM]	0.067	0.075	0.1
	[Combined]	0.64	0.37	0.11
$\frac{\mu}{2\Delta}$ (Rad)	[FVM]	0.99	1.2	1.3
	[Combined]	0.99	1.35	1.4
r_o (fm)	[FVM]	1.59	1.59	1.61
	[Combined]	1.6	1.59	1.62
d (fm)	[FVM]	0.013	0.02	0.03
	[Combined]	0.13	0.1	0. 32
$\lambda_\circ$		9.3	11.77	10.36
$\varphi_{\lambda_\circ}$ (deg)		50.33	53.74	38.45
$D_\circ$		1.645	38.15	36.7
$\Gamma_\circ$		12.01	43.8	48.25
R (fm)	[FVM]	8.41	8.41	8.52
	[Combined]	8.46	8.41	8.57
d/R	[FVM]	0.0015	0.0024	0.0035
	[Combined]	0.015	0.012	0.037
p	[FVM]	4.11	7.94	10.677
n	[FVM]	9.513	9.025	8.605
h	[FVM]	1.065	1.184	1.32
θ_R (Rad)	[FVM]	2.17	1.69	1.33
$\theta_{1/4}$ (Rad)	[Expt.]	2.077	1.58	1.34
$\theta_{\text{Nucl}}{}^{a}$ (Rad)	[FVM]	−7.4	−8.054	−6.44
σ_r (mb)	[GFM]	138.8	317.3	545.1
	[FM]	194.6	394.15	637.01
χ^2	[FVM]	8.76	13.19	26.02
	[Combined]	0.022	0.0078	0.0052

However, the combined model improves the quality of fittings by better reproducing the cross sections at backward angles.

Although the diffraction pattern of angular distribution of both processes is generally Fresnel type, both the experimental data and theoretical results exhibit some Fraunhofer oscillations. This is because the Coulomb effect is not strong enough to completely wash out the Fraunhofer oscillations. Moreover, the values of the diffusivity parameter, Δ, and the grazing angular momentum, Λ, from FVM are increasing with increasing energy as predicted by the strong absorption model. The quarter point angle, $\theta_{1/4}$, values are comparable to θ_R. The trend of change in the total reaction cross section for the two scattering processes with increasing laboratory energy is as expected.

The parameters $\lambda_\circ$, Γ_o and D_o which estimate the location of the pole, its amplitude and width, respectively, have an effect on moving the deepest minimum of angular distribution towards forward angles and on controlling the slope of the envelope of oscillations at backward angles. Due to the complicated and combined effect of these parameters of the Regge pole, any attempt to reproduce the precise number and size of experimental oscillations is rather a difficult task. Moreover, the parameter $\varphi_{\lambda_\circ}$ which represents the phase angle of the pole plays the role in determining the size of oscillations at backward angles but does not exhibit transparent behaviour upon the change in incident energy.

It is worth noting that the experimental data of angular distribution of ^{19}F + ^{18}O, ^{19}F + ^{16}O have almost the same number of oscillations at backward angles but the slope of envelope of angular distribution is different, as shown in Figs. 7 and 8. Due to SAM, the argument of getting the same number of oscillations may be justified by obtaining almost similar values of the pair (n, h) for the two systems. Moreover, for each of these systems when the projectile and target are swapped, the slope of the envelope of the new swapped system with a larger mass of projectile becomes steeper than the

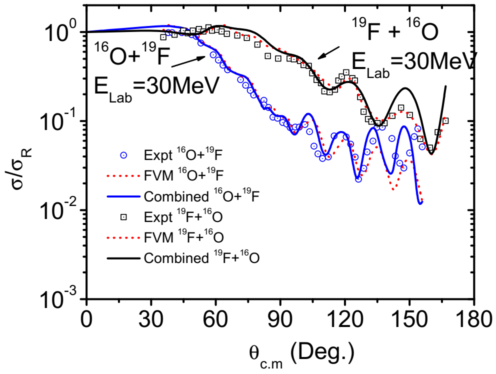

Fig. 7 Comparison of the angular distribution of the systems $^{16}O+{}^{19}F$ and $^{19}F+{}^{16}O$ at laboratory energy of 30 MeV

previous one which is justified by the values of Δ obtained from our analysis.

To summarise, it is found that the total reaction cross section σ_r increases with increasing laboratory energy (see Tables 5 and 6) for elastic scatterings $^{16}O+{}^{19}F$ and $^{18}O+{}^{19}F$, respectively, and as illustrated in Figs. 9 and 10 when both the GFM and simple FM are employed. σ_r is also increasing with the increase in the size of the projectile when incident energy and target nucleus are fixed (see Tables 1 and 2). Furthermore, σ_r is mildly changing when both the mass of the projectile nucleus and incident energy slightly increase (see Table 3).

4 Conclusions

The analyses of the available experimental data for the elastic scattering of $^{9,\,10,\,11}Be+{}^{64}Zn$ at laboratory energy of 27.95 MeV; $^{4,\,6,\,8}He+{}^{208}Pb$ at laboratory energy of 22 MeV; $^{18}O+{}^{19}F$, $^{16}O+{}^{19}F$ and $^{15}N+{}^{19}F$ at laboratory energies of 31.16, 30.4 and 25.95 MeV, respectively; $^{15}N+{}^{19}F$ at laboratory energies of 23, 26 and 29 MeV; $^{19}F+{}^{18}O$ at energies of 27, 30 and 33 MeV; and finally, $^{19}F+{}^{16}O$ at energies of 27, 30, 33 and 36 MeV, respectively, are carried out using the FVM. Our calculations reproduce the experimental angular distributions in the elastic scattering of strongly bound nuclei and halo nuclei at laboratory energies around the Coulomb barrier. The angular distribution present the typical Fresnel-type diffraction pattern of elastic scattering. The peaks that appear in our results belong to Fresnel patterns where rainbows do not exist in the case of elastic scattering of halo nuclei on targets with medium or heavy masses. The Coulomb interactions, however, have an effect on damping the Fraunhofer oscillations where the angular distribution becomes smoother with steeper slope in some cases. It is well-known that the elastic scattering of weakly bound nuclei on heavy targets is strongly affected by the polarisation induced by the dipole part of the Coulomb interaction. We believe that the significant reduction of cross sections in elastic scattering of weakly bound nuclei on heavy-ion targets may be ascribed to the effect of Coulomb dipole polarisability. This effect has been shown to account for part of the long range behaviour found in phenomenological OM analyses of these systems.

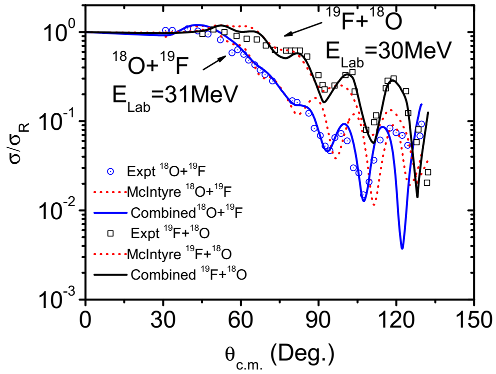

Fig. 8 Comparison of the angular distribution of the systems $^{18}O+{}^{19}F$ and $^{19}F+{}^{18}O$ at laboratory energies of 31 and 30 MeV, respectively

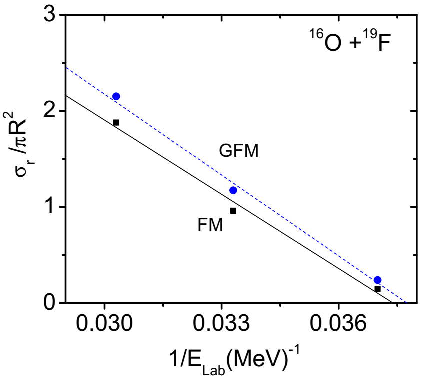

Fig. 9 The ratio $\frac{\sigma_r}{\pi R^2}$ versus the inverse of laboratory energy for $^{16}O+{}^{19}F$ elastic scattering, where the values of the total reaction cross section were found using the formulas provided by the simple Fresnel model (FM) and the generalised Fresnel model (GFM). Least square fits (*solid line*) for FM results and (*dashed line*) for GFM results are also shown

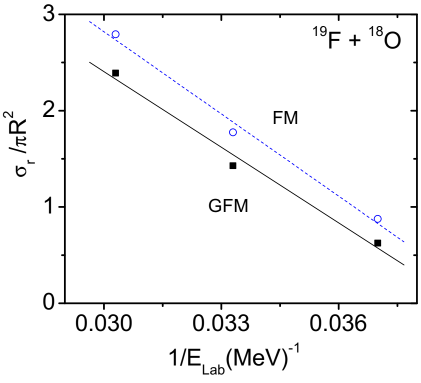

Fig. 10 The ratio $\frac{\sigma_r}{\pi R^2}$ versus the inverse of laboratory energy for $^{18}O+{}^{19}F$ elastic scattering, where the values of the total reaction cross section were found using the formulas provided by the generalised Fresnel model (GFM) and the simple Fresnel model (FM). Least square fits (*solid line*) for GFM results and (*dashed line*) for FM results are also shown

The correlation between the total reaction cross section and the nuclear halo structure for each scattering that involves the halo nucleus projectile is apparent, and values of total reaction cross section are found comparable with those of others. It is noted that the parameter *p* increases with the increase in the size of the projectile or target nucleus. It is also noted that the value of the ratio of the diffusivity parameter *d* to the interaction radius *R* provides a measure for the Coulomb damping of Fraunhofer oscillations in the shadow region.

The combined model, when the Regge pole factor is incorporated in the parameterised S-matrix, is also examined in order to recover some of the oscillatory structure of angular distribution at backward angles (if available). The Regge pole parameters play a role in adjusting the number of oscillations (if available) at backward angles. The combined complex role of the latter parameters makes the process of fitting very difficult, in some cases, to reproduce the correct number of experimental oscillations.

When the calculations of FVM give approximately similar values of the parameters (n, h) or (Λ, p) for two different elastic scattering processes, it is an indication that the description of strong absorption elastic scattering process using such parameterised model is model independent. Furthermore, deviations of some reproduced results from experimental data may be attributed to weak absorption and/or weakness due to several adopted approximations in the model.

References

1. W.E. Frahn, R.H. Venter, Ann. Phys. **24**, 243 (1963)
2. R.H. Venter, Ann. Phys. **25**, 405 (1963)
3. W.E. Frahn, Nucl. Phys. **75**, 577 (1966)
4. W.E. Frahn, Ann. Phys. **72**, 524 (1972)
5. W.E. Frahn, Nucl. Phys. A. **302**, 267 (1978)
6. R. I. Badran, A. I. Istaiti, W. N. Mashaqbeh, I. H. Al-Lehyani, Int. J. Mod. Phys. E 1550082 (2015). doi:10.1142/S0218301315500822
7. J.A. McIntyre, K.H. Wang, L.C. Becker, Phys. Rev. **117**, 1337 (1960)
8. J.A. McIntyre, S.D. Baker, K.H. Wang, Phys. Rev. **125**, 584 (1962)
9. H.A. Bethe, S.A. Kroff, G. Placzek, Phys. Rev. **57**, 573 (1940)
10. J.S. Blair, Phys. Rev. **95**, 1218 (1954)
11. J.S. Blair, Phys. Rev. **115**, 928 (1959)
12. J.S. Blair, D. Sharp, L. Wilets, Phys. Rev. **125**, 1625 (1962)
13. G.W. Farwell, H.E. Wagner, Phys. Rev. **93**, 356 (1966)
14. G.W. Farwell, W.E. Wegner, Phys. Rev. **95**, 1212 (1954)
15. K.R. Greider, A.E. Glassgold, Ann. Phys. **10**, 100 (1960)
16. N. Austern, J.S. Blair, Ann. Phys. **33**, 15 (1965)
17. R.I. Badran, H. Badahda, M. Arafah, R. Khalidi, Int. J. Mod. Phys. E. **19**, 2199 (2010)
18. R.I. Badran, D. Al-Masri, Can. J. Phys. **91**, 355 (2013)
19. R.I. Badran, H. Badahdah, J. Braz, Phys. Chem. Chem. Phys. **39**, 684 (2009)
20. R.I. Badran, D. Al-Masri, AIP. Proceed. **81**, 1569 (2013)
21. M.C. Mermaz, Zeitschrif. Fur. Physic. A. Hadrons Nuclei. **321**, 613 (1985)
22. R.I. Badran, D.J. Parker, I.M. Naqib, Euro. Phys. J. A. **12**, 317 (2001)
23. R.I. Badran, M.I. Naqib, D.J. Parker, J. Asher, J Phys. G. Nucl. Part. Phys. **22**, 1441 (1996)
24. M.C. Mermaz, Phys. Rev. C. **21**, 2356 (1980)
25. T. Regge, Nuovo Cimento, 14, 951 (1959); A. Bottino, A. M. Longoni, T. Regge, Nuovo Cimento, 23, 954 (1962)
26. L. Rebolia, G. A. Viano, Nuovo Cimento 26, 1426 (1962); M. Carrassi, G. Passatore, Nuovo Cimento 32, 1337 (1964); M. Bertero, M. Carrassi, G. Passatore, Nuovo Cimento 36, 954 (1965)
27. V. V. Grushin, Y. P. Nikitin, Sov. J. Nucl. Phys., 13, 89 (1971); V. V. Grushin, Y. P. Nikitin, Sov. J. Nucl. Phys., 5, 122 (1967)
28. A.A. Cowley, G. Heymann, Nucl. Phys. **A146**, 465 (1970)
29. U. Kiebele, E. Baumgartner, H.P. Gubler, H.O. Meyer, G.R. Plattner, I. Sick, Helv. Phys. Act. **51**, 726 (1978)
30. K.W. McVoy, Phys. Rev. C. **3**, 1104 (1971)
31. M.C. Mermaz, E.R. Chaves Lomlei, J. Barrette, B. Berthier, A. Greiner, Phys. Rev. C. **29**, 147 (1983)
32. C. Gruhn, N. Wall, Nucl. Phys. **81**, 161 (1966)
33. N. Austern, Ann. Phys. **15**, 299 (1961)
34. A. Di Pietro, G. Randisi, V. Scuderi, L. Acosta, F. Amorini, M.J.G. Borge, P. Figuera, M. Fisichella, L.M. Fraile, J. Gomez-Camacho, H. Jeppesen, M. Lattuada, I. Martel, M. Milin, A. Musumarra, M. Papa, M.G. Pellegriti, F. Perez-Bernal, R. Raabe, F. Rizzo, D. Santonocito, G. Scalia, O. Tengblad, D. Torresi, A. Maira Vidal, D. Voulot, F. Wenander, M. Zadro, Phys. Rev. Lett. **105**, 022701 (2010)
35. G. Marquínez-Durán, A.M. Sánchez Benítez, I. Martela, R. Berjillos, J. Dueñas, V.V. Parkar, L. Acosta, K. Rusek, M.A.G. Álvarez, J. Gómez-Camacho, M.J.G. Borge, C. Cruz, M. Cubero, V. Pesudo, O. Tengblad, A. Chbihi, J.P. Fernández-García, B. Fernández-Martínez, J.A. Labrador, A.H. Ziad, J.L. Flores, N. Keeley, L. Standylo, I. Strojek, M. Marques, M. Mazzocco, A. Pakou, N. Patronis, D. Pierroutsakou, R. Silvestri, R. Raabe, N. Soic, R. Wolski, Act. Phys. Pol. B. **43**, 239 (2012)
36. A.M. Sanchez Benitez, D. Escrig, M.A.G. Alvarez, M.V. Andres, C. Angulo, M.J.G. Borge, J. Cabrera, S. Cherubini, P. Demaret, J.M. Espino, P. Figuera, M. Freer, J.E. Garcia Ramos, J. Gómez Camacho, M. Gulino, O.R. Kakuee, I. Martel, C. Metelko, A.M. Moro, F. Pérez Bernal, J. Rahighi, K. Rusek, D. Smirnov, O. Tengblad, P. Van Duppen, V. Ziman, Nucl. Phys. A. **803**, 30 (2008)
37. J.P. Fernández-García, M. Rodríguez-Gallardo, M.A.G. Alvarez, A.M. Moro, Nucl. Phys. A. **840**, 19 (2010)
38. A. Bonaccorso, F. Carstoiu, Nucl. Phys. A. **706**, 322 (2002)
39. K. Rusck, N. Keely, K.W. Kemper, R. Raabe, Phys. Rev. C. **67**, 041604 (2003)
40. M. Cubero, J.P. Fernandez-Garcia, M. Rodriguez-Gallardo, L. Acosta, M. Alcorta, M.A.G. Alvarez, M.J.G. Borge, L. Buchmann, C.A. Diget, H. Al Falou, B.R. Fulton, H.O.U. Fynbo, D. Galaviz, J. Gomez-Camacho, R. Kanungo, J.A. Lay, M. Madurga, I. Martel, A.M. Moro, I. Mukha, T. Nilsson, A.M. Sanchez-Benitez, A. Shotter, O. Tengblad, P. Walden, Phys. Rev. Lett. **109**, 262701 (2012)
41. A. Gamp, W. von Oertzen, H.G. Bohlen, M. Feil, R.L. Walter, N. Marquardt, Z. Phys. **261**, 283 (1973)